

## Structural understanding of IrFe catalyst for renewable hydrogen production from ethanol steam reforming

Catherine KS Choong <sup>a</sup>, Yonghua Du <sup>b</sup>, Chee Kok Poh <sup>a</sup>, Sze Wei Daniel Ong <sup>a</sup>, Luwei Chen <sup>a,c,\*</sup>, Armando Borgna <sup>a</sup>

<sup>a</sup> Institute of Sustainability for Chemicals, Energy and Environment, Agency for Science, Technology, and Research (A\*STAR), 1 Pesek Rd., Jurong Island, 627833, Singapore

<sup>b</sup> National Synchrotron Light Source II, Brookhaven National Laboratory, Upton, NY 11973, USA

<sup>c</sup> Department of Materials Science and Engineering, National University of Singapore, 10 Kent Ridge Crescent, 119260, Singapore



### ARTICLE INFO

#### Keywords:

IrFe alloy  
Adsorption-induced  
Ethanol steam reforming  
Hydrogen  
XAS  
Hydrogen production

### ABSTRACT

Ethanol steam reforming (ESR) is an attractive way to produce renewable H<sub>2</sub> and has been intensely studied. An iron promoted Ir catalyst IrFe/Al<sub>2</sub>O<sub>3</sub> is reported for the first time to show better performance than Ir/Al<sub>2</sub>O<sub>3</sub> in ESR and the structural change in the IrFe/Al<sub>2</sub>O<sub>3</sub> catalyst under realistic ESR conditions is investigated. IrFe alloy is observed after reduction in H<sub>2</sub>. However, the IrFe alloy is disrupted during ESR because of an adsorption-induced structural change. Ir appears in metallic-like state while Fe exists as partially reduced Fe<sub>x</sub>O<sub>y</sub> under the reaction condition. The active center is therefore IrFe<sub>x</sub>O<sub>y</sub> instead of IrFe alloy. The discovery of the transformation of IrFe alloy to IrFe<sub>x</sub>O<sub>y</sub> during ESR deepens the understanding of the dynamic behaviour of IrFe catalyst and provides a correlation between the catalyst structure and catalytic performance.

### 1. Introduction

Ethanol (EtOH) steam reforming (ESR, CH<sub>3</sub>CH<sub>2</sub>OH + 3 H<sub>2</sub>O → 2CO<sub>2</sub> + 6 H<sub>2</sub>) is attractive for the production of renewable H<sub>2</sub>, which can be used as clean energy [1,2]. Thermal efficiency of 86% can be achieved with the integration of ESR with in situ CO<sub>2</sub> separation [2]. ESR can be operated within a temperature range of 300 to 800 °C, with its functionality classified into two categories: low-temperature ESR and high-temperature ESR. Catalysts based on transition and noble metals such as Ni, Co, Rh, Pt have been intensively studied for both high temperature and low temperature ESR [3]. However, few studies have focused on Ir-based catalysts although Ir belongs to the same group in the periodic table as Rh [4,5]. Previously, we reported that iron can enhance hydrogen production and most importantly, lower CO selectivity over RhFe/Al<sub>2</sub>O<sub>3</sub> catalysts at low temperature ESR [6–8]. In this work, we report the effect of iron on IrFe/Al<sub>2</sub>O<sub>3</sub> catalysts for ESR and the investigation of active sites for the IrFe/Al<sub>2</sub>O<sub>3</sub> catalyst.

The promotional effect of Fe on Ir catalysts has been reported in several catalytic reactions. Takakazu Fukushima and Masaru Ichikawa et al. reported significant increment in activity and MeOH selectivity by

adding Fe to Ir/SiO<sub>2</sub> (Fe:Ir = 0.2), similar to the promotional effect of Fe on Rh for the CO hydrogenation to methanol [9,10]. Results of Mossbauer experiments on IrFe/SiO<sub>2</sub> reduced at 400 and 500 °C demonstrate that iron exists either as Fe<sup>3+</sup> or Fe<sup>0</sup> clusters with Ir particles [11]. A later study by Koningsberger et al. pointed out that there may have been a transformation of the bimetallic IrFe active phases in iron-rich Ir catalyst during time-on-stream reaction [12]. The active phase was proposed to be a two-site interaction of IrFe<sup>3+</sup> for CO hydrogenation to methanol [13]. Fe was also found to promote the CO oxidation reaction of Ir via weakening the CO adsorption and enhanced oxygen activation by the oxygen vacancies by iron oxides in the close contact with Ir [14]. Since Ir and Fe have very good miscibility in bulk, IrFe alloy has been observed in several reports [14–17]. In a recent study, the nanoparticles of IrFe composites were prepared by the reduction of Ir and Fe precursors using NaBH<sub>4</sub> in liquid phase. By varying the Ir to Fe molar ratio from 4:1 to 1:4, IrFe alloy, a mixture of IrFe alloy with Fe<sub>2</sub>O<sub>3</sub> and metallic Ir with Fe<sub>2</sub>O<sub>3</sub> were synthesized [17]. Other alloys such as PdFe, PtRe, IrNi, RhFe and PtNi catalysts were reported [8,18–22]. Evidently, the structure of multicomponent catalysts greatly depends on catalyst preparation, ratio of the elements and reduction conditions. The alloy structure can change

\* Corresponding author at: Institute of Sustainability for Chemicals, Energy and Environment, Agency for Science, Technology, and Research (A\*STAR), 1 Pesek Rd., Jurong Island 627833, Singapore.

E-mail address: [chen\\_luwei@isce2.a-star.edu.sg](mailto:chen_luwei@isce2.a-star.edu.sg) (L. Chen).

**Table 1**

List of some literature focusing on the reduction of CO selectivity.

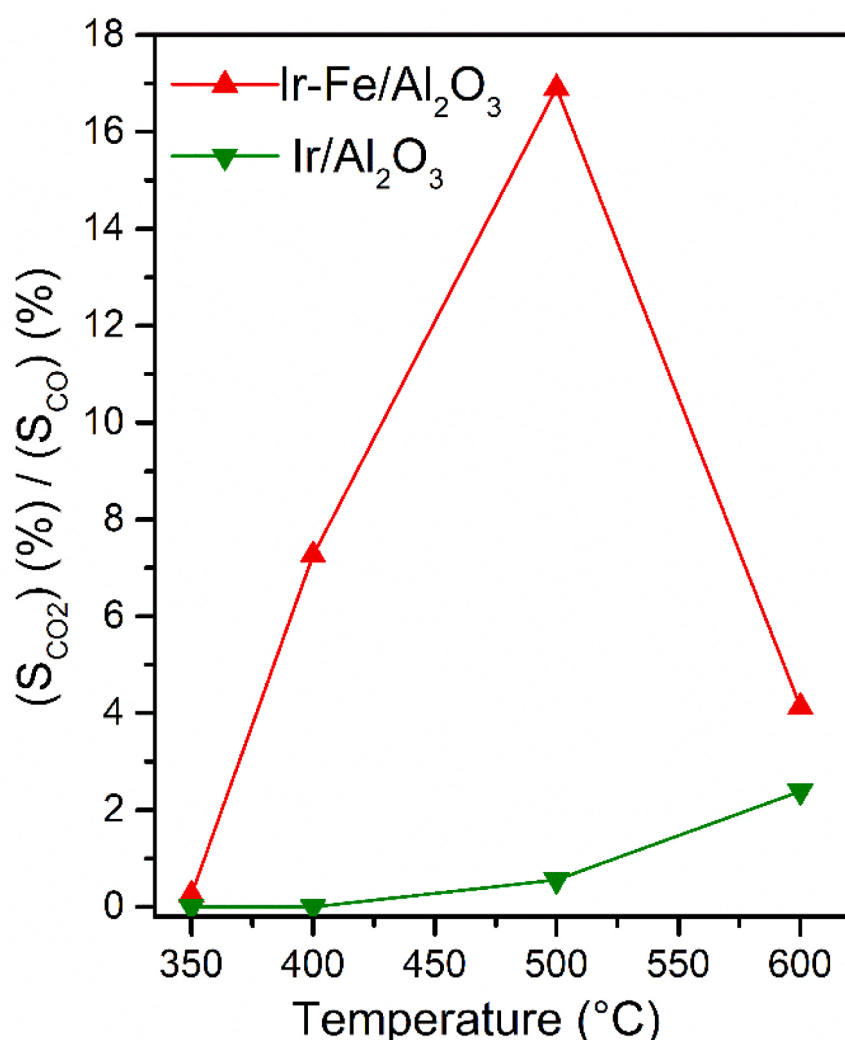
Catalyst	T (°C)	GHSV (h <sup>-1</sup> )	EtOH:H <sub>2</sub> O (molar)	EtOH	YH <sub>2</sub> (mol)	S <sub>CO</sub> (%)	Ref.
				Conv. (%)			
1%Rh10Fe %-/Ca-Al <sub>2</sub> O <sub>3</sub>	350	30,000	1:10	100	4.14	0	[6]
10 wt% Co/ZnO	350	5000	1:13	100	5.42	0	[25]
		20,000		100	na	1.1	
		30,000		100	na	2.9	
0.98%Na10% CoZn	350	5000	1:13	100	5.48	0.4	[26]
Fe <sub>0.15</sub> Co <sub>2.85</sub> O <sub>4</sub>	400	5200	1:06	100	n.a.	0.2	[27]
1.5%Pt/Ce <sub>0.8</sub> Zr <sub>0.2</sub> O <sub>2</sub>	400	30,000	1:05	100	1.99	1.5	[28]
2%Rh/Ce <sub>0.8</sub> Zr <sub>0.2</sub> O <sub>2</sub>	450	85,320	1:08	100	4.3	11.0	[29]

depending on the reaction conditions. Therefore, analysis of catalysts under *in situ* conditions is crucial to reveal the real active sites and their transformation during catalytic reactions. As such, better correlation of catalytic performance to active sites can be achieved.

ESR is a complex reaction in which dozens of side reactions are involved [23,24]. During the reaction, the reactant H<sub>2</sub>O may behave as an oxidizer thereby oxidizing the reduced metal species. On the other

hand, the H<sub>2</sub> produced from ethanol steam reforming acts as a reducing agent. In addition, CO produced in the reaction can strongly adsorb on metal surface resulting in the poisoning of the active sites, therefore reducing the selectivity of CO to enhance the production of H<sub>2</sub> and extending the life of catalyst attracts a lot of intention [6]. Some examples of studies of this nature are shown in Table 1 [25–29]. Since high temperature is not favourable for WGS, high selectivity of CO is typically observed. *In situ* XPS study by N. J. Divins et al. discloses the migration of Pd towards the surface of RhPd bimetallic nanoparticles during reduction and the partial oxidation of both Rh and Pd under operating condition of ESR at 550 °C [30]. However, at low temperature ESR, Rh catalyst is deactivated by CO adsorption [6]. A dynamic change in the structure of the catalysts due to the adsorption of the reactants during real operating conditions is expected especially for bimetallic/alloy catalysts which have differing properties from the two metals [31].

Identifying and understanding the origin of the active sites is essential for the interpretation of catalytic activity data and for the purpose of advancing catalyst design and improvement. However, the studies of the catalyst under real operating conditions are scarce [30]. In this study, a series of *in situ* studies by X-ray absorption fine structure (XAFS) spectroscopy under simulated ESR conditions reveal interesting structure changes on IrFe/Al<sub>2</sub>O<sub>3</sub>, are presented.

**Fig. 1.** S<sub>CO2</sub>/S<sub>CO</sub> as a function of temperature measured during ESR.

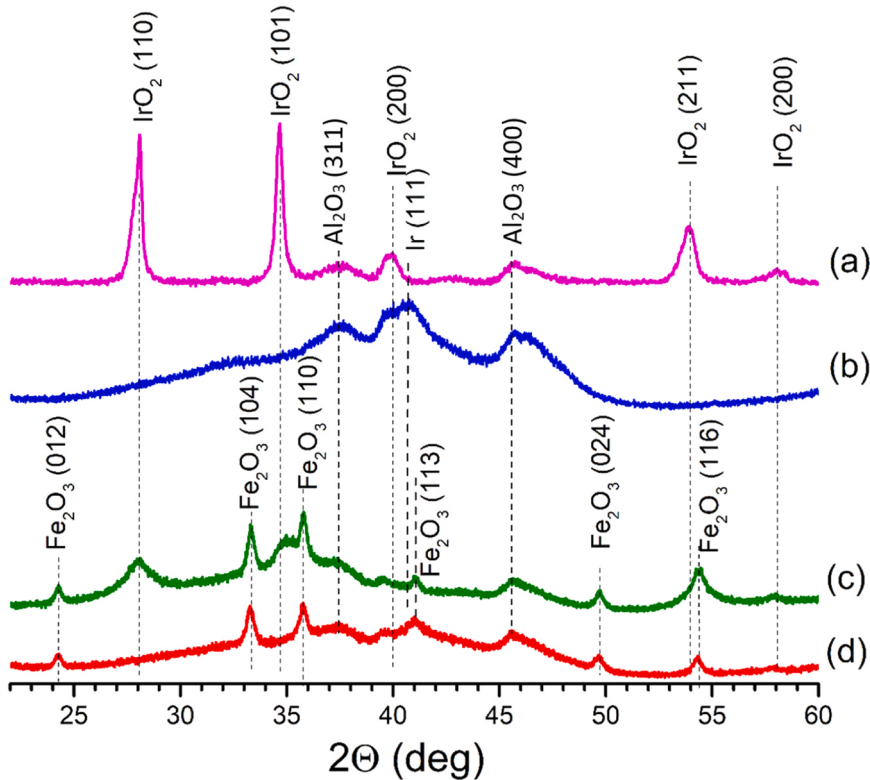


Fig. 2. XRD spectra of (a) Ir/Al<sub>2</sub>O<sub>3</sub>; (b) Ir/Al<sub>2</sub>O<sub>3</sub> reduced at 250 °C. (c) Ir-Fe/Al<sub>2</sub>O<sub>3</sub> and (d) Ir-Fe/Al<sub>2</sub>O<sub>3</sub> reduced at 250 °C.

## 2. Experimental

### 2.1. Catalyst synthesis

To synthesis IrFe/Al<sub>2</sub>O<sub>3</sub> catalyst, stoichiometric amount of iron (III) nitrate nonahydrate (Sigma-Aldrich, Fe(NO<sub>3</sub>)<sub>3</sub>.9 H<sub>2</sub>O) was dissolved in deionized water and added dropwise into aluminum oxide (Merck,  $\gamma$ -Al<sub>2</sub>O<sub>3</sub>) powder. The mixture was thoroughly mixed to obtain a homogenous paste mixture. The paste was dried at 100 °C for 2 h and calcined at 500 °C for 5 h. Deposition precipitation method was used to load iridium onto the synthesized Fe-promoted support. The procedure is as follows: the calcined Fe/Al<sub>2</sub>O<sub>3</sub> powder was dispersed in 500 mL deionized water containing stoichiometric amount of hexachloroiridic acid hexahydrate H<sub>2</sub>IrCl<sub>6</sub>.6 H<sub>2</sub>O (Sigma-Aldrich, 99.98% metal basis) at room temperature. The mixture was heated to 75 °C under stirring and 0.2 M Na<sub>2</sub>CO<sub>3</sub> aqueous solution was gradually added to the solution until a final value of pH 10 was achieved. The slurry was further aged for 3 h at 75 °C before filtrating and washing with water and ethanol. Subsequently, the sample was dried at 120 °C for 2 h before calcination at 500 °C for 5 h. The catalyst is denoted as IrFe/Al<sub>2</sub>O<sub>3</sub> where the composition of Ir and Fe is 4% and 11% by weight, respectively. The Fe-free Ir/Al<sub>2</sub>O<sub>3</sub> with 4% weight loading of Ir was prepared using the same method.

### 2.2. Catalytic measurements

The catalytic evaluation was performed using a fixed-bed reactor. 100 mg of catalyst, sandwiched between quartz wool, was loaded into a stainless steel (1/8' OD) reactor tube. Heating was provided by a Carbolite tube furnace, and the temperature of each sample was monitored electronically via a thermocouple located within the reactor. Prior to each run, the catalyst sample was reduced in 10% H<sub>2</sub>/He mixture (50 mL/min) at 250 °C for 1 h with a heating ramp rate of 10 °C/min. Upon completion of the reduction process, the catalyst was cooled in pure argon (Ar) (50 mL/min) until the desired reaction temperature has

been reached for activity measurements.

For activity measurements, 40 mL/min of Ar was introduced into the reactor, along with 0.005 mL/min of ethanol-water mixture (EtOH:H<sub>2</sub>O = 1:3 by volume or 1:9.6 by molar basis), delivered by a Shimadzu Liquid Pump. The feed line was heated at 150 °C to vaporize the ethanol and water before the mixture passes through the reactor. The concentration of ethanol in the gas phase (Ar+H<sub>2</sub>O+EtOH) is 15.3% and the total GHSV of 88000 mL g<sup>-1</sup>h<sup>-1</sup>. The outlet of the reactor was also heated at 150 °C to avoid condensation of liquid products. The reaction products were analyzed online using a gas chromatograph (Varian CP-3800) with three columns: Porapak Q, Haysep Q and molecular sieve 5 A. Porapak Q was used to separate organics and carbon dioxide with He as carrier gas, while the other two columns were used for the separation of hydrogen, carbon monoxide and methane with Ar as carrier gas. The products were analyzed using two thermal conductivity detectors. The ethanol conversion (X<sub>EtOH</sub>) and selectivity to carbon containing species (S<sub>Ci</sub>) were calculated based on Eqs. 1 and 2, respectively:

$$X_{EtOH} (\%) = \frac{mol \text{ of } EtOH_{in} - mol \text{ of } EtOH_{out}}{mol \text{ of } EtOH_{in}} \times 100 \quad (1)$$

$$S_{C_i} (\%) = \frac{mol \text{ of } C_i}{\sum_i^n mol \text{ of } C_i} \times 100 \quad (2)$$

where C<sub>i</sub> represents a C-containing product. The selectivity S<sub>Ci</sub> was calculated based on detected carbon species only, assuming that no coke was formed during the reaction. H<sub>2</sub> yield (Y<sub>H2</sub>) was evaluated in terms of the number of moles of H<sub>2</sub> produced per mole of fed ethanol. The results reported here are generally obtained after 10 min of time-on-stream and the values were averaged over 1.5 h of time-on-stream.

### 2.3. Catalyst characterization

X-ray diffraction (XRD) spectra were collected at room temperature using a Bruker D8 Advance diffractometer (Bruker AXS GmbH,

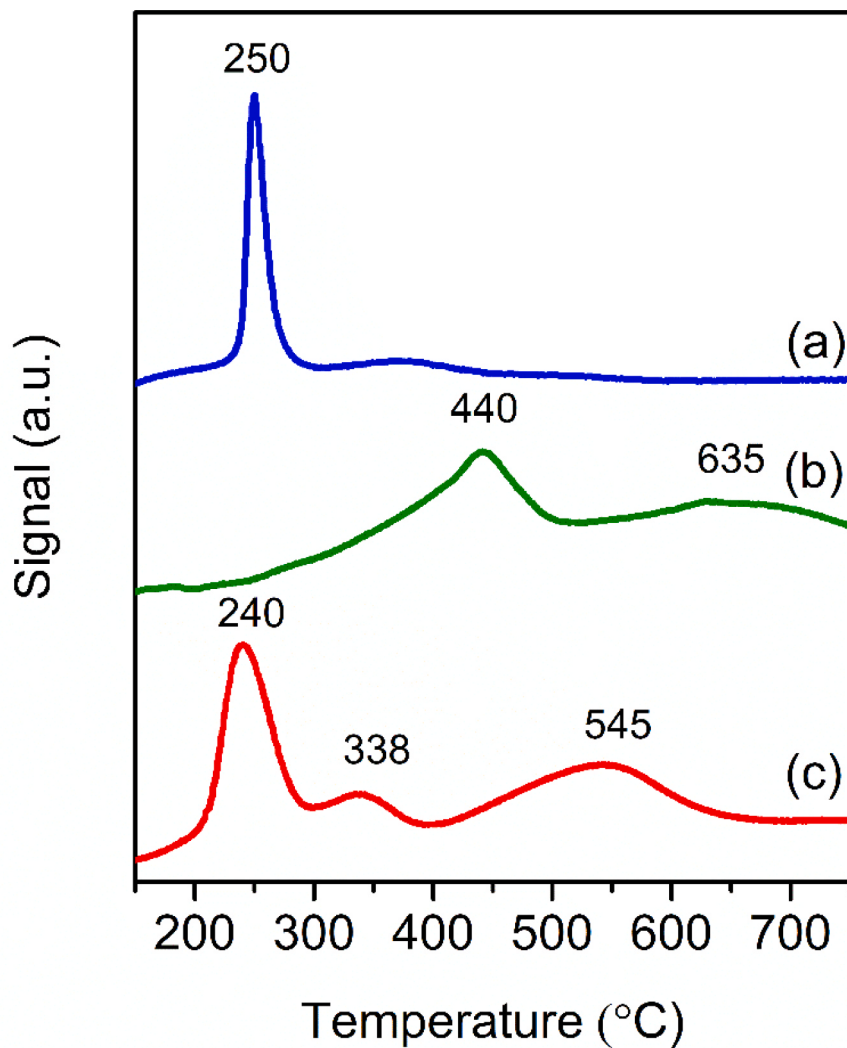


Fig. 3. TPR profiles of (a) Ir/Al<sub>2</sub>O<sub>3</sub>; (b) Fe/Al<sub>2</sub>O<sub>3</sub> and (c) IrFe/Al<sub>2</sub>O<sub>3</sub>.

Germany) equipped with Cu-K $\alpha$  radiation source ( $\lambda = 1.54056 \text{ \AA}$ ) operated at 40 kV and 30 mA. The samples were scanned within the range of Bragg's angle ( $2\Theta$ ) = 10° to 90°. Surface areas were measured by a Micromeritic ASAP2420, using the multi-point BET method.

Temperature programmed reduction (TPR) was conducted using the Thermo Electron Corporation TPDRO 1100 Series Catalyst Analyzer unit equipped with a thermal conductivity detector (TCD). Catalyst sample mass of 50 mg were used. The sample was heated up in 50 mL/min of flowing 5% H<sub>2</sub>/Ar with a temperature ramp rate of 15 °C/min from 30 up to 750 °C. The H<sub>2</sub> consumption is detected via a thermal conductivity detector (TCD).

XPS was performed using ESCALAB 250 spectrometer and Al K $\alpha$  was used as the X-ray source. For the analysis of a reduced sample, the sample was reduced at 250 °C for 1 h in H<sub>2</sub>. Narrow scans for the Ir 4 f, Fe 2p and Al 2p peaks was performed and the charging of the samples was corrected by referencing all energies to the Al 2p peak at 74 eV. A Gaussian-Lorentzian procedure was used for curve fitting of peaks by XPSPEAK. The Transmission electron microscopy (TEM) micrographs of the reduced catalysts were taken using Fei Tecnai G2 TF20 S-twin microscope.

#### 2.4. In situ X-ray adsorption fine structure (XAFS) spectroscopy

The XAFS spectroscopy experiments were carried out at XAFCA beamline of Singapore Synchrotron Light Source [32]. The beamline has

a flux of  $1.6 \times 10^{10}$  photons per second at 7 keV and covers the photon energy range from 1.2 keV to 12.8 keV, making use of two sets of monochromator crystals, a Si(111) crystal for the range from 2.1 to 12.8 keV and a KTiOPO<sub>4</sub> crystal (KTP(011)) for the range between 1.2–2.8 keV. The energy resolution was about  $5.1 \times 10^{-4}$  at 10 keV.

In situ XAFS spectroscopy measurements were carried out using wafer samples (I.D. 10 mm pellets) under transmission mode. The disc of 10 mm (ID) containing 50 mg of catalyst mixed with boron nitride for Ir and Fe scan. Measurements of the as-calcined catalyst were collected at 30 °C in 100 mL/min of He. The catalyst was reduced at 250 °C for 0.5 h and measurements were taken in H<sub>2</sub>. Finally, temperature was increased to 300 °C and held for 0.5 h where a mixture of EtOH+H<sub>2</sub>O was fed with the same composition and flow rate as the activity test. In another experiment to study the effect of CO adsorption on the structure of IrFe/Al<sub>2</sub>O<sub>3</sub> catalyst, the catalyst was reduced at 250 °C in H<sub>2</sub>, followed by adsorption of CO at 350 °C. Fe and Ir standard were applied for the energy calibration. Data processing was performed using the Demeter package [32].

### 3. Results and discussions

#### 3.1. Catalytic results

The ethanol conversion and product distribution of Ir/Al<sub>2</sub>O<sub>3</sub> (BET surface area:155 m<sup>2</sup> /g) and IrFe/Al<sub>2</sub>O<sub>3</sub> (BET surface area:124 m<sup>2</sup> /g)

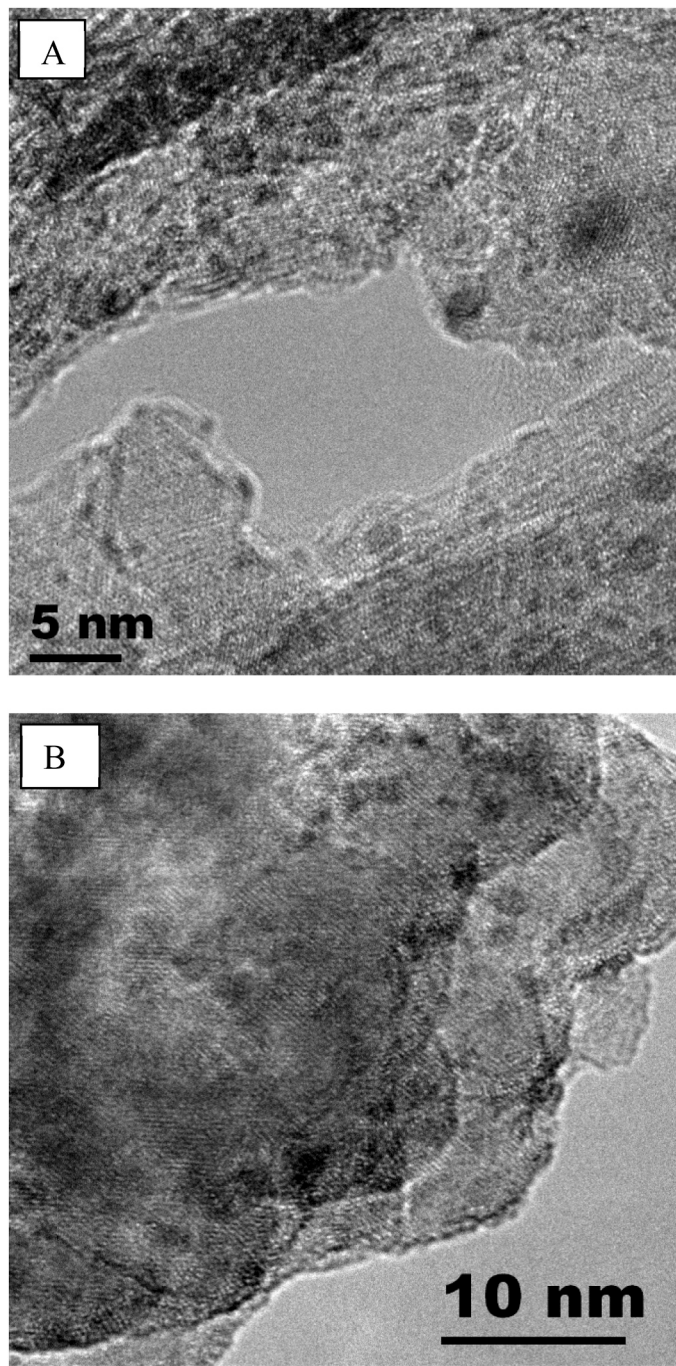


Fig. 4. TEM micrographs of reduced Ir/Al<sub>2</sub>O<sub>3</sub> (A) and IrFe/Al<sub>2</sub>O<sub>3</sub> (B).

reduced at 250 °C are shown in Table 1. The catalytic performance of IrFe/Al<sub>2</sub>O<sub>3</sub> for ESR is superior to the monometallic Ir/Al<sub>2</sub>O<sub>3</sub>. There is a marked increase in ethanol conversion when the Ir/Al<sub>2</sub>O<sub>3</sub> catalyst is promoted with Fe, especially at the low temperature 350–400 °C. On Ir/Al<sub>2</sub>O<sub>3</sub> catalyst, Ir is deactivated rapidly by adsorption of CO by-product, leading to the production of CH<sub>3</sub>CHO as the major product [4,7]. Dehydrogenation of ethanol to CH<sub>3</sub>CHO is generally accepted as the first step reaction in ESR [33]. In contrast, IrFe is effective in breaking C–C bond and converting them into other products such as H<sub>2</sub>, CO<sub>2</sub>, CO and CH<sub>4</sub>. In addition, a plot of S<sub>CO2</sub>/S<sub>CO</sub> in Fig. 1 vs temperature shows that S<sub>CO2</sub>/S<sub>CO</sub> is constantly higher for IrFe in comparison to Ir. This suggests that the presence of Fe can effectively enhance the water gas shift reaction (WGSR), an observation similar to RhFe catalyst reported by our group [6]. We observed ethanol is first adsorbed and activated at Rh

active sites. In the presence of Fe<sub>x</sub>O<sub>y</sub>, the CO which adsorbed onto the Rh particles can migrate from Rh to the nearby Fe<sub>x</sub>O<sub>y</sub> where it is further converted to CO<sub>2</sub> via WGSR [6]. In addition, the partially reduced Fe<sub>x</sub>O<sub>y</sub> also facilitates the activation of H<sub>2</sub>O for WGSR. Similarly, in a study of IrFe/Al<sub>2</sub>O<sub>3</sub> catalyst for preferential CO oxidation, metallic Ir is responsible for CO adsorption and O<sub>2</sub> is active on Fe<sub>x</sub>O<sub>y</sub> sites [34]. Analogous to our previous study on RhFe for ESR and IrFe for CO oxidation reaction, IrFe/Al<sub>2</sub>O<sub>3</sub> is believed to undergo the same reaction mechanism where the catalytic performance of the catalyst depends on the availability of IrFe<sub>x</sub>O<sub>y</sub> sites. A decrease in S<sub>CO2</sub>/S<sub>CO</sub> for IrFe catalyst at temperatures higher than 500 °C, suggests the WGSR is not favourable at high temperature, though a structural change of IrFe<sub>x</sub>O<sub>y</sub> sites at higher reaction temperature is also possible. To elucidate the structural changes of IrFe/Al<sub>2</sub>O<sub>3</sub> under working conditions, the following sections will present the analysis of XRD and TPR, results along with in situ structural characterizations were performed using XAFS spectroscopy under H<sub>2</sub> reduction, ethanol steam reforming and CO adsorption.

### 3.2. XRD, TPR and TEM

Fig. 2 shows the X-ray diffraction (XRD) patterns of as-calcined and reduced Ir/Al<sub>2</sub>O<sub>3</sub> and IrFe/Al<sub>2</sub>O<sub>3</sub> catalysts. The characteristic diffraction peaks at 28.1°, 34.7°, 39.9° and 53.9° corresponding to those of IrO<sub>2</sub> (PDF#43–1019) are observed in the as-calcined Ir/Al<sub>2</sub>O<sub>3</sub> XRD pattern. However, in the IrFe/Al<sub>2</sub>O<sub>3</sub> catalyst, the IrO<sub>2</sub> diffraction peaks are less pronounced and broader compared to those in the pattern of the Ir/Al<sub>2</sub>O<sub>3</sub> catalyst. This suggests a better dispersion of Ir particles with the introduction of Fe because the interaction between IrO<sub>2</sub> and Al<sub>2</sub>O<sub>3</sub> is weakened by the presence of iron oxide. The average crystal size of the calcined catalysts, calculated based on IrO<sub>2</sub> (110) peak at 28.1° using the Scherrer's equation, are 15.6 and 7.5 nm for Ir/Al<sub>2</sub>O<sub>3</sub> and IrFe/Al<sub>2</sub>O<sub>3</sub>, respectively. The peaks of iron oxide on IrFe/Al<sub>2</sub>O<sub>3</sub> belong to the  $\alpha$  phase Fe<sub>2</sub>O<sub>3</sub> (PDF#33–0664). Therefore, both Ir and Fe exist as IrO<sub>2</sub> and Fe<sub>2</sub>O<sub>3</sub> on the calcined catalysts. No new crystalline phases were observed.

The interaction between Ir and Fe on IrFe/Al<sub>2</sub>O<sub>3</sub> is clearly exhibited during the reduction procedure, reflected by the changes of IrO<sub>2</sub> and Fe<sub>2</sub>O<sub>3</sub> TPR reduction peaks as shown in Fig. 3. A major single and symmetric peak of H<sub>2</sub> consumption at 250 °C is observed on Ir/Al<sub>2</sub>O<sub>3</sub>, suggesting most of the supported IrO<sub>2</sub> particles experience the one step reduction from IrO<sub>2</sub> to metallic Ir. The TPR of Fe/Al<sub>2</sub>O<sub>3</sub> shows two broad H<sub>2</sub> consumption peaks at 440 and 635 °C, with the former one relatively more intense than the latter one as shown in Fig. 3(b). These two reduction peaks correspond to the reduction from Fe<sub>2</sub>O<sub>3</sub> → Fe<sub>3</sub>O<sub>4</sub> → Fe in the Fe/Al<sub>2</sub>O<sub>3</sub> sample. The reduction peak of IrO<sub>2</sub> on IrFe/Al<sub>2</sub>O<sub>3</sub> appears at 240 °C, 10 °C, lower than that of IrO<sub>2</sub> on Ir/Al<sub>2</sub>O<sub>3</sub>. The ease of reduction of IrO<sub>2</sub> on iron promoted IrFe/Al<sub>2</sub>O<sub>3</sub> suggests smaller IrO<sub>2</sub> particles than those on Ir/Al<sub>2</sub>O<sub>3</sub> [34]. This result agrees with the conclusion derived from XRD where smaller IrO<sub>2</sub> particle size is observed in IrFe/Al<sub>2</sub>O<sub>3</sub> compared to Ir/Al<sub>2</sub>O<sub>3</sub>. The reduction of Fe<sub>2</sub>O<sub>3</sub> on IrFe/Al<sub>2</sub>O<sub>3</sub> also becomes easier than Fe/Al<sub>2</sub>O<sub>3</sub> due to the active H spill over from reduced Ir to the Fe<sub>2</sub>O<sub>3</sub> in close vicinity.

The reduction of IrO<sub>2</sub> is also clearly observed from the XRD study on the reduced Ir/Al<sub>2</sub>O<sub>3</sub> and IrFe/Al<sub>2</sub>O<sub>3</sub> (Figs. 2b and 2d). IrO<sub>2</sub> diffraction peaks (110) at 28.2°, (200) at 58.3° and (310) at 65.9° disappear after the reduction at 250 °C for one hour. Metallic Ir peaks are invisible except for the most intense Ir (111) peak, which appears as a broad and weak peak, indicating that the reduced Ir species are highly dispersed on the reduced catalysts. Diffraction peaks of Fe<sub>2</sub>O<sub>3</sub> (110) at 35.8°, (116) at 54.3° and Al<sub>2</sub>O<sub>3</sub> peak at 67.2° become sharper and more symmetric because other IrO<sub>2</sub> peaks appearing as shoulders of Fe<sub>2</sub>O<sub>3</sub> such as IrO<sub>2</sub> (101) at 35.0°, (211) at 53.8° in the calcined IrFe/Al<sub>2</sub>O<sub>3</sub> also disappear. Therefore, combining the TPR and XRD results, we can conclude that the IrO<sub>2</sub> phase disappears, most probably due to the formation of small metallic species which are undetectable by XRD, while nano Fe<sub>2</sub>O<sub>3</sub> particles remain present after reduction. TEM micrograph in Fig. 4 A shows most of the Ir nanoparticles are less than 3 nm. As for IrFe/Al<sub>2</sub>O<sub>3</sub>

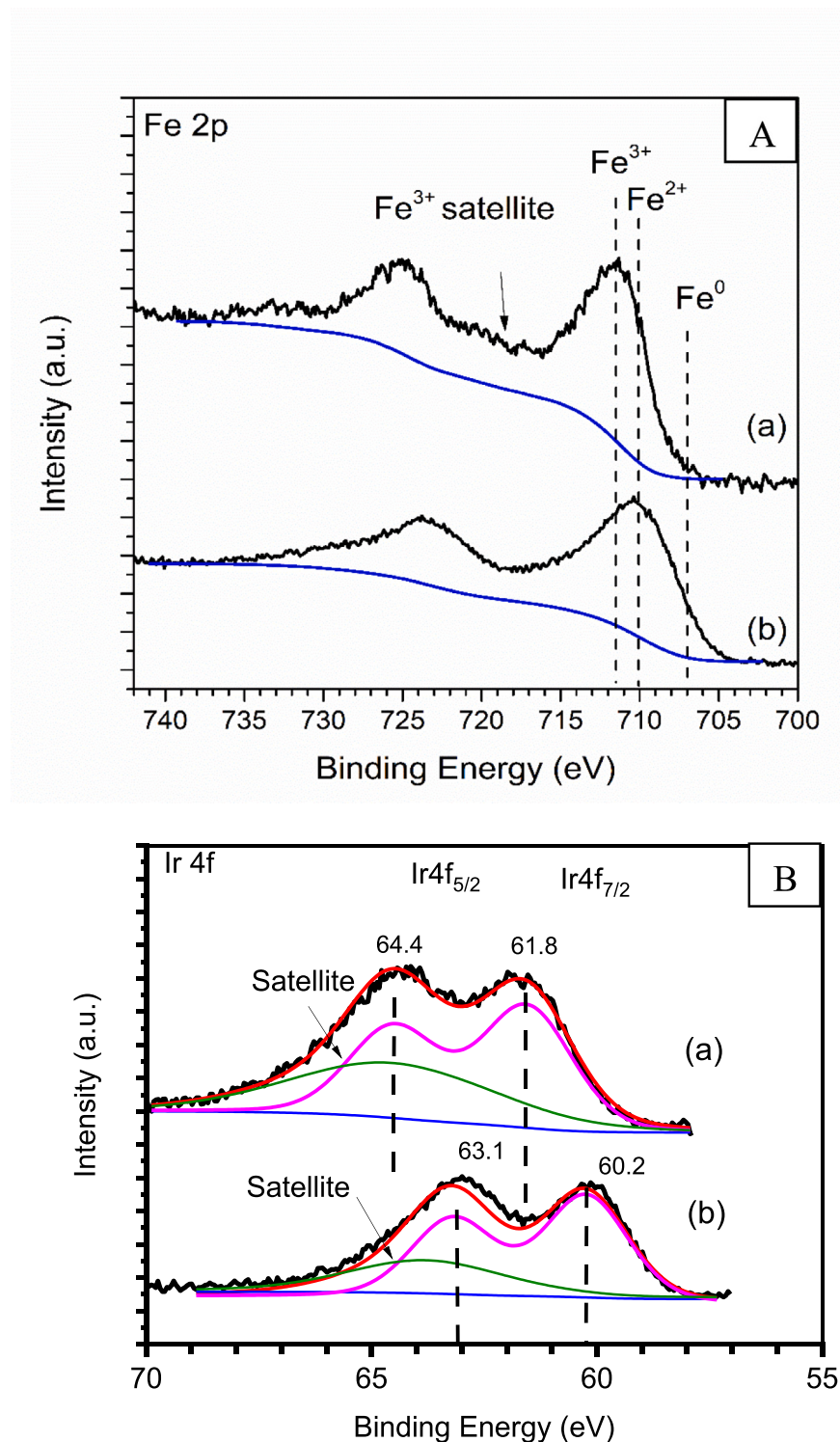
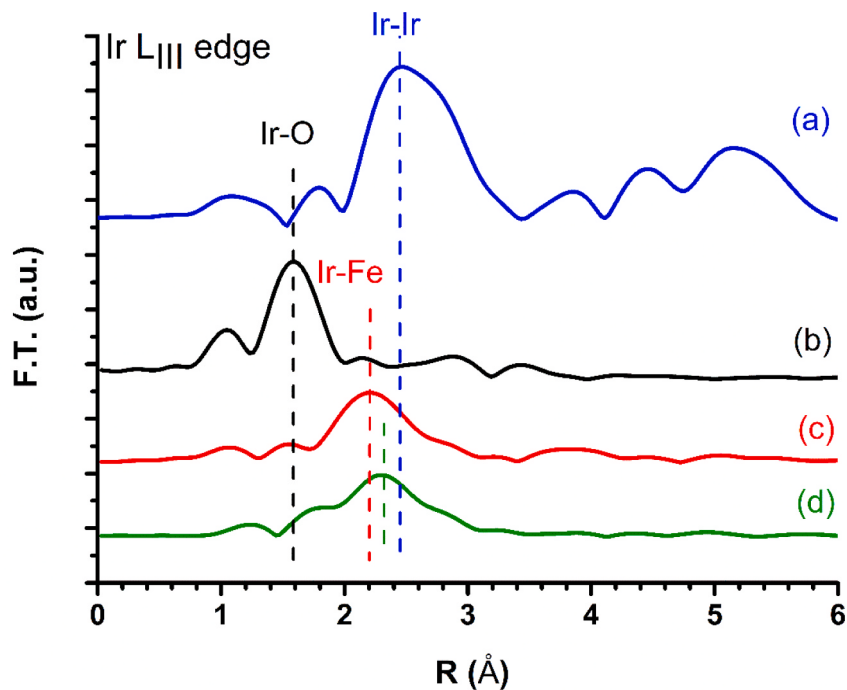


Fig. 5. XPS analysis of (A) Fe 2p and (B) Ir 4 f of as-calcined (a) and reduced (b) IrFe/Al<sub>2</sub>O<sub>3</sub> (at 250 °C for an hour).

in Fig. 4 B, although the overall Ir particles are in the same range of Ir/Al<sub>2</sub>O<sub>3</sub>, boundaries of Ir particles are not very clear due to the interaction between Ir and Fe.

It is also noteworthy that the width of the diffraction peak  $2\Theta$  value at  $41.1^\circ$ , which corresponds to Fe<sub>2</sub>O<sub>3</sub> (113) plane, broadens. In addition, its intensity is higher than the previous Fe<sub>2</sub>O<sub>3</sub> (113) in the calcined IrFe/Al<sub>2</sub>O<sub>3</sub>. It is thus reasonable to suspect this peak at  $41.1^\circ$  in the reduced IrFe/Al<sub>2</sub>O<sub>3</sub> is not only contributed by Fe<sub>2</sub>O<sub>3</sub> (113). As the metallic Ir (111) peak is at  $40.7^\circ$  (PDF#06-0598), the formation of metallic Ir or

IrFe alloy is probable after reduction. The blue shift of the diffraction angle indicates the shrinking of lattice structure due to the intercalation of Fe atom which has smaller radii than Ir atom [17]. Although only Fe<sub>2</sub>O<sub>3</sub> phase is detected by XRD, the reduction of iron oxide can be observed from the shift in Fe 2p<sub>3/2</sub> binding energy from 711.8 eV to lower binding energy (in Fig. 5A) which corresponds to iron species of lower oxidation states. The disappearance of Fe<sup>3+</sup> satellite peak at 718 eV on the reduced IrFe/Al<sub>2</sub>O<sub>3</sub> using XPS is also another indication of iron oxide reduction. Binding energies of Ir 4 f<sub>7/2</sub> of calcined and



**Fig. 6.** Fourier transforms of Ir L<sub>III</sub>-edge EXAFS spectra of the IrFe/Al<sub>2</sub>O<sub>3</sub> at different stages: as-calcined (b); reduced at 250 °C (c); ESR at 300 °C (d) and iridium foil (a).

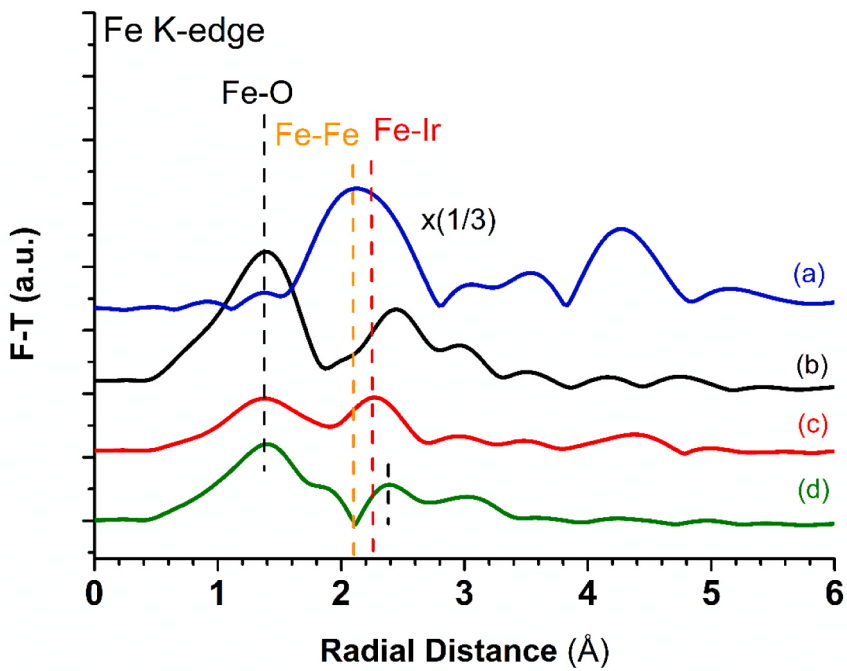


**Fig. 7.** Fourier transforms of Fe K-edge EXAFS spectra of the IrFe/Al<sub>2</sub>O<sub>3</sub> different stages: as-calcined (b); reduced at 250 °C (c); ESR at 300 °C (d) and iron foil (a).

reduced catalyst appear 61.8 and 60.2 eV, corresponding to Ir in the state of IrO<sub>2</sub> and Ir, respectively [35]. **Fig. 5 (B)**The above XPS and XRD results all prove the co-existing of metallic Ir, metallic Fe and iron oxides in the reduced IrFe/Al<sub>2</sub>O<sub>3</sub> catalyst. As the reliability of XRD is influenced by its dependence on long-range order, the presence of less crystalline structures may not be apparent. Hence, we also employed XAFS spectroscopy, which is capable of detecting both crystalline and amorphous structures, in our characterization. The following XAFS results on the in situ reduction and ethanol steam condition will provide more information on the structures of the proposed IrFe nanoalloy.

### 3.3. In-situ XAFS spectroscopy

#### 3.3.1. XAFS study of the catalyst reduction

**Fig. 6** shows the  $k^2$ -weighted Fourier transforms of Ir EXAFS spectra of the as-calcined IrFe/Al<sub>2</sub>O<sub>3</sub> sample, and the sample reduced under H<sub>2</sub> at 250 °C along with iridium foil as reference. To note, the distance scale in the Fourier transformed spectra is not corrected for phase shift. The Fourier-transformed EXAFS spectrum at the Ir L<sub>III</sub>-edge of the as-calcined IrFe/Al<sub>2</sub>O<sub>3</sub> catalyst depicts a peak at 1.60 Å corresponding to IrO bond. Reduction of the catalyst under hydrogen at 250 °C changes

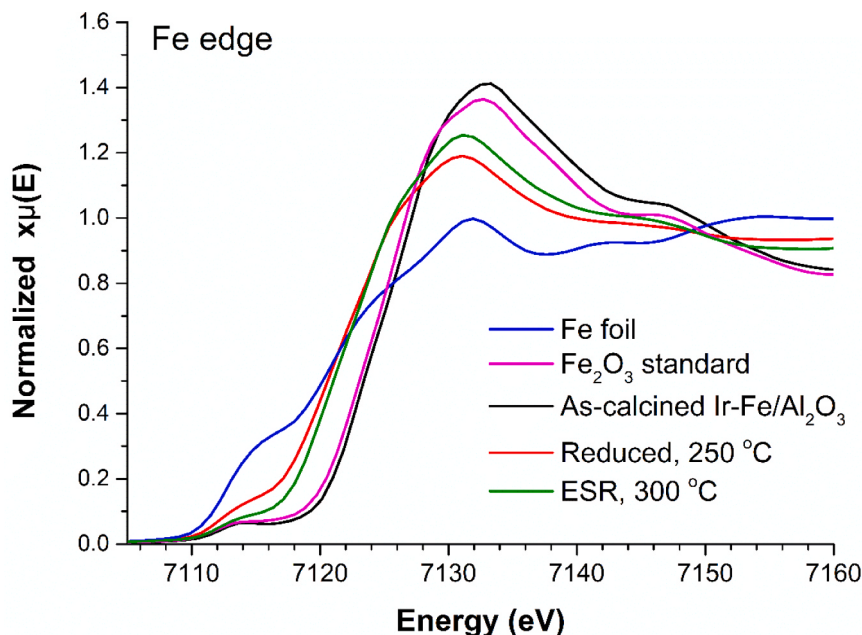


**Fig. 8.** In situ Fe K-edge XANES spectra of the IrFe/Al<sub>2</sub>O<sub>3</sub> under different atmosphere. Fe and Fe<sub>2</sub>O<sub>3</sub> foil are used as references.

the structure of the catalyst significantly. First, a marked decrease in the IrO scattering intensity at 1.60 Å as compared to the as-calcined sample is observed, indicating the reduction of IrO<sub>2</sub>. Consistent with results from XRD, XPS and TPR, IrO<sub>2</sub> is reduced under H<sub>2</sub> environment. Second, a significantly higher signal is observed at 2.20 Å which is significantly shorter than the standard Ir-Ir peak position of 2.46 Å (without phase correction) in Ir foil standard but it cannot be associated to IrO coordination. Such a phenomenon was similarly observed in the NiIr and FeRh alloy [19,21]. In a NiIr<sub>x</sub>/Al<sub>2</sub>O<sub>3</sub> bimetallic catalyst reduced at 300 °C, the distance between the absorber and backscatter atoms was found to be shorter than the Ir-Ir distance [19]. Since Ir has larger atomic radii than Fe, it is reasonable to propose the red shift of the interatomic distance from the foil standard indicates the intermixing of Ir and Fe, or IrFe alloy formation after reduction.

Complementing the Ir L<sub>III</sub>-edge data, Fe K-edge EXAFS spectrum taken under H<sub>2</sub> atmosphere at 250 °C in Fig. 7 also shows the presence of FeIr alloy phase at a bond distance of 2.20 Å. In addition, a decrease in Fe-O scattering intensity at 1.39 Å, which indicates the reduction of Fe<sub>2</sub>O<sub>3</sub>, is observed. The reduction of Fe<sub>2</sub>O<sub>3</sub> agrees with the results from Fe K-edge XANES of reduced IrFe/Al<sub>2</sub>O<sub>3</sub> (Fig. 8). The reduced sample shows a decrease in the white line intensity and a downward shift in the absorption edge position from 7124 to 7122 eV when compared with the as-calcined IrFe/Al<sub>2</sub>O<sub>3</sub>.

Although the analysis presented above clearly points out the alloy formation upon reduction, we have further analysed the XAS data to prove that indeed Ir-Fe alloy formation takes place. Hence, an inverse Fourier transform was applied over a restricted range of R, isolating the EXAFS contribution of the first coordination shell of iridium. The EXAFS functions were modelled using phase shifts and back scattering amplitudes obtained from both theoretical standards and reference compounds. Fig. 9 clearly shows that the experimental data of the reduced catalyst are only well fitted by considering the simultaneous presence of Ir-Ir and Ir-Fe distances. Table 2 summarizes the fittings parameters, including the R-factor to assess the goodness of the fittings. The alloy formation is clearly demonstrated.

The formation of IrFe alloy has previously been reported in IrFe/SiO<sub>2</sub> catalysts in hydrogenation of CO and preferential oxidation of CO using EXAFS and Mössbauer spectroscopy [14,16]. According to Ferrando et al., there are four possible existing patterns of a bimetallic/alloy system, i.e.: (1) core-shell segregated nanoalloys; (2) subcluster

segregated nanoalloys consisting of A and B metal subclusters with sharing interface; (3) mixed A-B nanoalloys and (4) multishell nanoalloys may present layered or onion-like alternating -A-B-A- shells [36]. The results above clearly demonstrate a consistent IrFe bond length such that we can confirm the presence of IrFe alloy on reduced IrFe/Al<sub>2</sub>O<sub>3</sub> resembles the A-B mixed structure nanoalloy.

### 3.3.2. In situ XAFS under ESR

In previous studies, some alloys formed during reduction remain in alloy state while, in some cases, the alloy structure change depending on reaction conditions [9–12,14,16]. In order to investigate the stability of the IrFe alloy observed in this paper and to correlate the catalytic behaviour with the structure of the IrFe/Al<sub>2</sub>O<sub>3</sub> catalyst, ethanol and steam were introduced into the chamber at 300 °C after reduction. The Fourier transformed Ir EXAFS spectrum under ESR in Fig. 6(d) is characterized by a shift in the main peak from 2.20 Å to 2.31 Å, as compared to the reduced catalyst in Fig. 6(c). This shift to higher radial distance towards IrIr distance of Ir foil (2.46 Å), indicates the partial disruption of IrFe alloy under reaction conditions.

To further investigate this, we performed the fittings of the first coordination shell. Fig. 10, along with Table 3, clearly show that the experimental data under ESR conditions are only well fitted by considering the simultaneous presence of Ir-Ir and Ir-Fe distances. However, the Ir-Fe coordination decreases, confirming the partial disruption of the Ir-Fe alloy. The slight decrease of the coordination number may indicate that the alloy disruption only occurs on the surface and on the outermost shells of the alloy nanoparticles. From EXAFS of Fe K-edge (Fig. 7), Fe-Ir peak at 2.25 Å diminished in the presence of ESR reactants at 300 °C. Therefore, the EXAFS data collected at both the Ir L<sub>III</sub> and Fe K edges unambiguously indicate the disruption of IrFe in IrFe/Al<sub>2</sub>O<sub>3</sub> during ESR reaction. The interpretation of Fe-O scattering from Fe K-edge EXAFS spectrum is complicated as it involves the interaction of Fe with Al<sub>2</sub>O<sub>3</sub> support as well as iron oxide species of a different valence. Nevertheless, Fe K-edge EXAFS spectrum of working IrFe/Al<sub>2</sub>O<sub>3</sub> catalyst under ESR bears a resemblance to the calcined sample, indicating reoxidation of the iron species. A clear picture of re-oxidation of iron species can be seen from the slight positive shift in the absorption edge position and an increase in white line intensity under ESR conditions from Fe K-edge XANES spectrum in Fig. 8.

Previously, we reported that iron can enhance hydrogen production

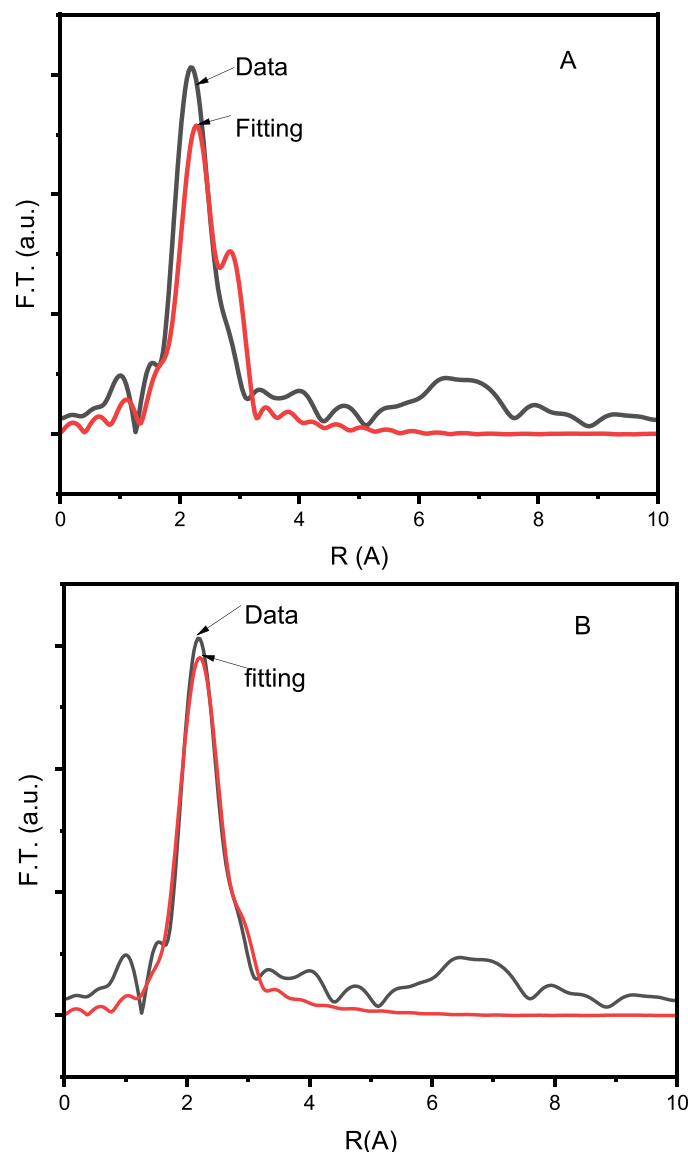


**Fig. 9.** Fittings in R-space of EXAFS data at Ir  $L_{3,4}$ -edge for Ir-Fe catalyst reduced at. (a) Fitting considering only Ir-Ir coordination, (b) Fitting considering both Ir-Ir and 250  $^{\circ}\text{C}$  Ir-Fe coordination.

and most importantly lower CO selectivity over RhFe/Al<sub>2</sub>O<sub>3</sub> catalyst at low temperature ESR [6–8]. Similar results were obtained as shown in paper when IrFe/Al<sub>2</sub>O<sub>3</sub> was used. Earlier research by our group demonstrated the formation of RhFe interfacial sites using a series of ex situ and in situ characterization tools such as XRD, DRIFTS, XAFS spectroscopy etc. However, this is the first time our catalyst was examined under realistic working conditions where ESR reactants were

introduced into the chamber of XAFS spectroscopy. These newly minted results not only reinforce our previous findings that Fe<sub>x</sub>O<sub>y</sub> are present but also reveal structural changes on IrFe/Al<sub>2</sub>O<sub>3</sub> during the reduction and reaction process. The IrFe alloy, formed during reduction, undergoes disruption during ESR, resulting in the formation of Ir clusters and oxidized iron oxide species, such as Fe<sub>x</sub>O<sub>y</sub>. The former helps in the C-C bond break in ethanol while the latter can quickly convert the adsorbed CO on Ir via WGSR. Our findings are very similar to that of Lu et al. who performed qualitative analysis of different Fe species in IrFe/SiO<sub>2</sub> under various gas compositions using Mössbauer spectroscopy and found that IrFe alloy can be oxidized into Fe<sup>2+</sup> species during CO oxidation with the aid of H<sub>2</sub> [14].

### 3.3.3. *In situ* XAFS under CO

Based on the above results, we can conclude that IrFe alloy is formed under H<sub>2</sub> at 250  $^{\circ}\text{C}$  before ESR. However, the IrFe alloy structure was disrupted under ESR at 350 to 500  $^{\circ}\text{C}$ . This disruption is likely caused by its interaction with reactants and products from ESR, consistent with reports on adsorption-induced structural and oxidation state changes on metal surfaces in heterogeneous catalysis [37]. In particular, CO is one of the most common molecules responsible for the structural change for both single metal and alloy. The EXAFS study by Prins et al. on the adsorption of CO on highly dispersed Rh crystallites supported on Al<sub>2</sub>O<sub>3</sub> observed the disruption of a significant number of Rh-Rh bonds [38]. Later FTIR studies by Solymosi et al. on Al<sub>2</sub>O<sub>3</sub> supported Rh and Ir catalysts reported oxidative fragmentation of Ir<sub>x</sub> crystallites and the formation of Rh<sup>I</sup>(CO)<sub>2</sub> and Ir<sup>I</sup>(CO)<sub>2</sub> carbonyl [39,40]. The morphological changes induced by CO adsorption on Rh was imaged at atomic scale and subcarbonyl Rh<sup>0</sup>(CO)<sub>2</sub> was proposed as the precursor of carbonyl previously observed by Kruse et al. [41]. Meanwhile, in bimetallic/alloy catalysts, it was found that the less active transition metals such as Ni in Pt<sub>3</sub>Ni(111) and Fe in IrFe alloy (IrFe/SiO<sub>2</sub>) can be partially oxidized into Pt-NiO<sub>1-x</sub> and IrFeO during CO oxidation reaction [14,22]. Analogous to the above examples, CO, a by-product from dissociation of ethanol in ESR reaction, is probably one of the reasons for the breaking of Ir-Fe bond observed in Figs. 6 and 7. To verify this hypothesis, EXAFS was carried out after CO adsorption at 350  $^{\circ}\text{C}$  on the reduced IrFe/Al<sub>2</sub>O<sub>3</sub> catalyst. As shown in Fig. 11(a), the peak at 2.32  $\text{\AA}$  diminishes upon the CO adsorption for 30 min. In the meantime, the peak of Ir-Fe in the reduced catalyst shifts slightly towards to standard Ir-Ir peak after CO exposure in Fig. 11(b). We propose that CO is adsorbed on Fe and subsequently oxidizes Fe to iron oxide. This is a logical explanation for the drastic decrease in the IrFe alloy peak in the FT EXAFS of Fe K-edge spectrum. On the contrary, Ir may still remain metallic as there is no IrO bonding peak observed at shorter distance in Fig. 11(b). Ir may exists as small Ir clusters containing only a few atoms due to the shorter Ir-Ir distance compared to Ir foil. The shorter metal-metal distance in dimer or very small metal cluster than in standard bulk metal-metal distance have been reported for Pt<sub>2</sub> dimer and small clusters. Some simulation works concluded the Pt-Pt in a Pt dimer has bond length of 2.4  $\text{\AA}$  to 2.6  $\text{\AA}$ , shorter than the Pt-Pt bond length of 2.77  $\text{\AA}$  in bulk Pt [42–44]. In addition, experimental work also demonstrates that two-dimensional Pt rafts with fewer than ten Pt atoms and

**Table 2**  
Activity of catalysts from 350 to 600  $^{\circ}\text{C}$ .

T ( $^{\circ}\text{C}$ )	Catalyst	Y <sub>H2</sub> (H <sub>2</sub> /EtOH mol/mol)	X <sub>EtOH</sub> (%)	S <sub>CO2</sub> (%)	S <sub>CO</sub> (%)	S <sub>CH4</sub> (%)	S <sub>C2H4</sub> (%)	S <sub>CH3CHO</sub> (%)	Others (%)
350	Ir/Al <sub>2</sub> O <sub>3</sub>	0.3	45.2	0	1.6	2.3	0	96.1	0
	Ir-Fe/Al <sub>2</sub> O <sub>3</sub>	3.2	99.8	7.5	29.5	24.2	1	37.9	0
400	Ir/Al <sub>2</sub> O <sub>3</sub>	0.6	62	0	4.8	4.9	0	90.4	0
	Ir-Fe/Al <sub>2</sub> O <sub>3</sub>	4.1	100	52.7	7.3	36.7	0.8	0	2.5
500	Ir/Al <sub>2</sub> O <sub>3</sub>	2.5	87.4	3.1	5.5	3.3	5.9	82.2	0
	Ir-Fe/Al <sub>2</sub> O <sub>3</sub>	4.4	100	61.3	3.6	35.1	0	0	0
600	Ir/Al <sub>2</sub> O <sub>3</sub>	5.4	100	40.5	43.4	7.4	4.9	3.8	0
	Ir-Fe/Al <sub>2</sub> O <sub>3</sub>	5.5	100	71.1	17.2	11.7	0	0	0

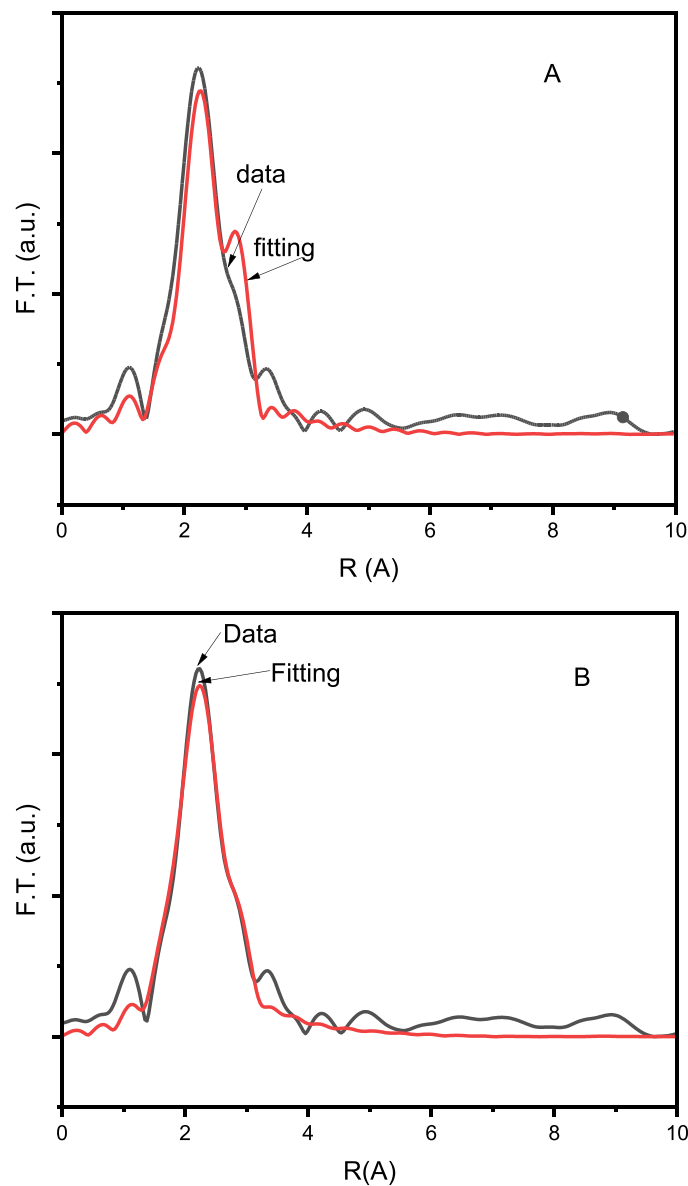


**Fig. 10.** Fittings in R-space of EXAFS data at Ir L<sub>3,3</sub>-edge for Ir-Fe catalyst under ESR conditions at 300 °C. (a) Fitting considering only Ir-Ir coordination, (b) Fitting considering both Ir-Ir and Ir-Fe coordination.

**Table 3**  
EXAFS results of XAS spectra measured at room temperature after reduction under H<sub>2</sub> at 250 °C.

Fittings	Bond	N	R (Å)	$\sigma^2$ (Å <sup>2</sup> )	R-Factor
Only Ir-Ir coordination	Ir-Ir	10.4 ± 3.9	2.71*	0.0117 ± 0.0039	0.143
Both Ir-Ir and Ir-Fe coordination	Ir-Fe	6.3 ± 0.6	2.56 ± 0.03	0.0122 ± 0.0012	0.013
	Ir-Ir	2.7 ± 0.3	2.71*	0.0024 ± 0.0003	

\* Parameter fixed when performing the fittings.

three-dimensional Pt clusters of size  $\leq 1$  nm have the Pt-Pt distance 2.53 Å and coordination number 3.8 only [45].

Therefore, the disruption of IrFe alloy under ESR condition can be due to the adsorption of the reaction by-product CO. It has been found that CO adsorption causes less reactive alloy components to segregate to

**Table 4**

EXAFS results of XAS spectra measured at room temperature after ESR at 300 °C.

Fittings	Bond	N	R (Å)	$\sigma^2$ (Å <sup>2</sup> )	R-Factor
Only Ir-Ir coordination	Ir-Ir	11.1 ± 2.7	2.71*	0.0126 ± 0.0027	0.071
Both Ir-Ir and Ir-Fe coordination	Ir-Fe	4.9 ± 0.5	2.56 ± 0.03	0.0187 ± 0.0019	0.016
	Ir-Ir	3.1 ± 0.3	2.71*	0.0055 ± 0.0006	

\* Parameter fixed when performing the fittings.

the surface [31]. Correspondingly Fe in IrFe alloy can migrate to the surface and be oxidized into Fe<sub>x</sub>O<sub>y</sub> by CO adsorption and come into close contact with Ir. Density functional theory show that the energy gain from CO binding to low-coordinated Cu atoms and the weakening of binding of Cu to neighboring atoms help drive this process [49]. The Ir-Fe<sub>x</sub>O<sub>y</sub> then serves as the active center for the ESR reaction similar to the mechanism, proved previously on Re-Fe catalyst [6]. Structural model of the IrFe/Al<sub>2</sub>O<sub>3</sub> catalyst after reduction and in ESR is proposed in [Scheme 1](#).

#### 4. Conclusions

In summary, IrFe/Al<sub>2</sub>O<sub>3</sub> shows higher activity and selectivity to H<sub>2</sub> than monometallic Ir/Al<sub>2</sub>O<sub>3</sub> in ethanol steam reforming for hydrogen production. TPR and XRD results suggest there is interaction between Ir and Fe. Strong evidence from in situ XAFS spectroscopy experiment indicate IrFe alloy can be formed after reduction at 250 °C. However, the alloy is disrupted when the catalyst is exposed to the reactants, i.e., the mixture of ethanol and steam. The disruption of IrFe alloy also occurs upon CO adsorption. Therefore, the adsorption induced structural change by CO adsorption could be the reason for the disruption of alloy in ESR. Fe in the original IrFe alloy is oxidized while small clusters of Ir remain when the alloy is disrupted. The real catalytic center is thus postulated to be Ir-Fe<sub>x</sub>O<sub>y</sub> instead of IrFe alloy.

For future research into this IrFe/Al<sub>2</sub>O<sub>3</sub> catalyst, studies should focus on the long term stability of the IrFe/Al<sub>2</sub>O<sub>3</sub> catalyst. It is important to look into the regeneration of the active centre if the regeneration is required. Ir:Fe ratio can be further optimized to enhance the efficiency of Ir to increase the sustainability of the overall process. Other factors such as the effect of water and ethanol on IrFe alloy disruption and the morphological changes of IrFe nano-alloy upon CO, ethanol and steam adsorption will be studied in greater details to yield deeper insights into the fundamental attribute of bimetallic catalyst.

#### CRediT authorship contribution statement

**Chen Luwei:** Conceptualization, Investigation, Supervision, Validation, Writing – review & editing. **Choong Catherine KS:** Data curation, Investigation, Methodology, Writing – original draft. **Ong Sze Wei Daniel:** Formal analysis, Investigation. **Borgna Armando:** Supervision, Validation, Writing – review & editing. **Du Yonghua:** Formal analysis, Investigation, Methodology, Validation. **Poh Chee Kok:** Formal analysis, Investigation, Writing – review & editing.

#### Declaration of Competing Interest

The authors declare that they have no known competing financial interests or personal relationships that could have appeared to influence the work reported in this paper.

#### Data Availability

No data was used for the research described in the article.

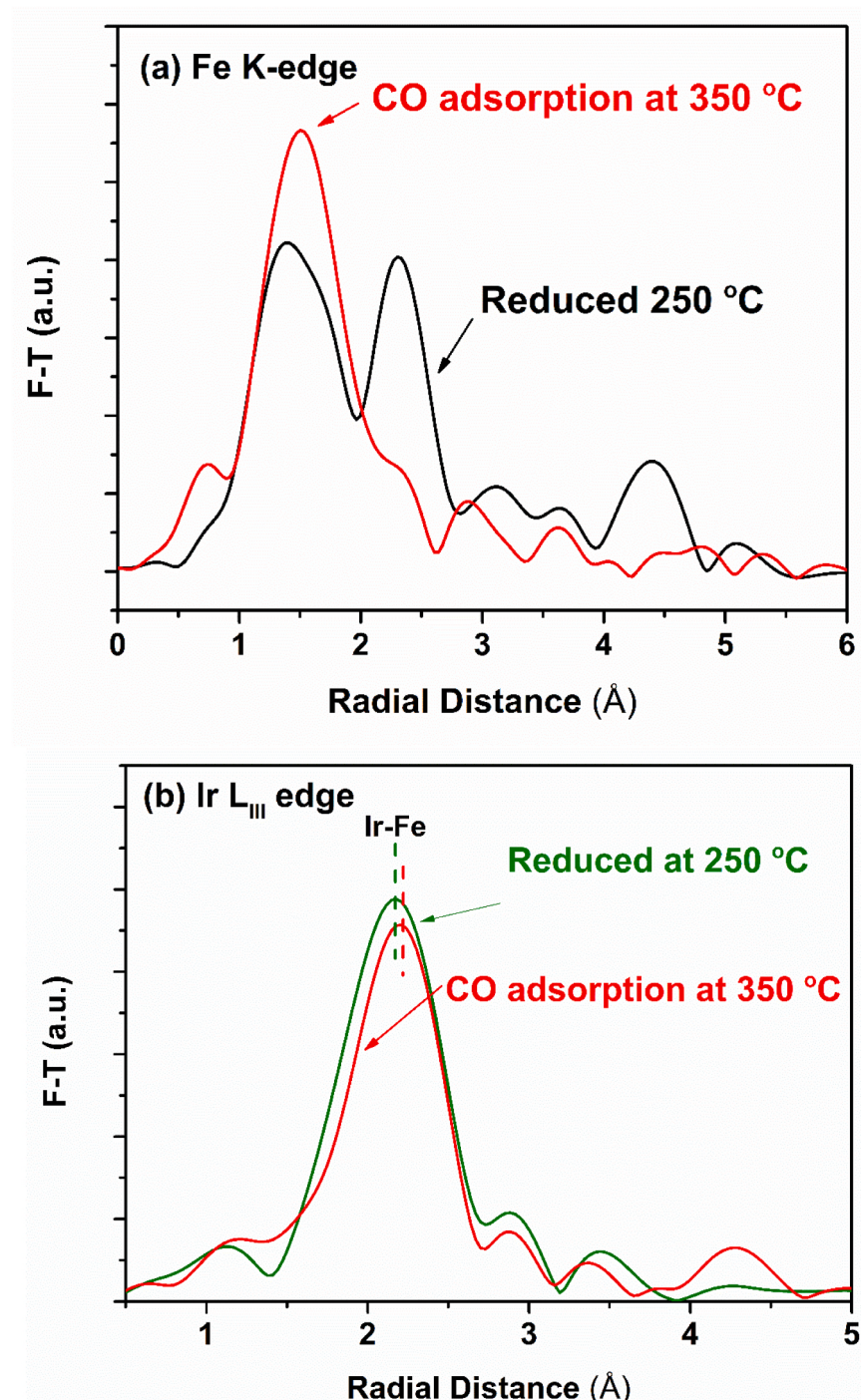
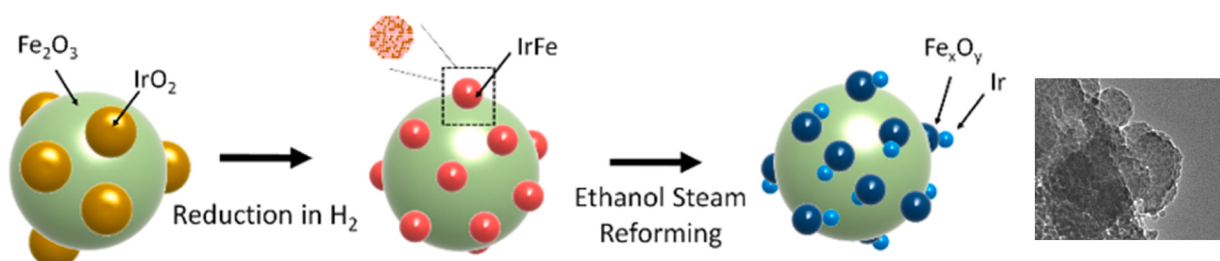


Fig. 11. Fourier transforms of (a) Fe K-edge and (b) Ir L<sub>III</sub>-edge EXAFS spectra of Ir-Fe/Al<sub>2</sub>O<sub>3</sub> at 250 °C in H<sub>2</sub> and at 350 °C in CO.



Scheme 1. Schematic illustration of the structural evolution under reduction and ethanol steam reforming reaction.

## Acknowledgment

The authors thank the Science and Engineering Research Council of A\*STAR (Agency for Science Technology and Research), Singapore, for financial support, Joel Tan, Bas Terlingen and Zhan Wang for their help in the catalytic performance, TEM and XPS measurements, respectively.

## References

- [1] D.K. Liguras, D.I. Kondarides, X.E. Verykios, Production of hydrogen for fuel cells by steam reforming of ethanol over supported noble metal catalysts, *Appl. Catal. B Environ.* 43 (2003) 345–354.
- [2] N. Saupsor, P. Kasempremchit, P. Bumroongsakulsawat, S. Kim-Lohsoontorn, W. Wongsakulphasatch, N. Kiatkittipong, J. Laosiripojana, S. Gong, Assabumrungrat, Performance comparison among different multifunctional reactors operated under energy self-sufficiency for sustainable hydrogen production from ethanol, *Int. J. Hydrol. Energy* 45 (2020) 18309–1832.
- [3] F. Auprétre, C. Descorme, D. Duprez, Bio-ethanol catalytic steam reforming over supported metal catalysts, *Catal. Comm.* 3 (2002) 263–267.
- [4] W. Cai, F. Wang, E. Zhan, A.C. Van Veen, C. Mirodatos, W. Shen, Hydrogen production from ethanol over Ir/CeO<sub>2</sub> catalysts: a comparative study of steam reforming, partial oxidation and oxidative steam reforming, *J. Catal.* 257 (2008) 96–107.
- [5] W. Cai, F. Wang, C. Daniel, A.C. van Veen, Y. Schuurman, C. Descorme, H. Provendier, W. Shen, C. Mirodatos, Oxidative steam reforming of ethanol over Ir/CeO<sub>2</sub> catalysts: a structure sensitivity analysis, *J. Catal.* 286 (2012) 137–152.
- [6] L. Chen, C.K.S. Choong, Z. Zhong, L. Huang, T.P. Ang, L. Hong, J. Lin, Carbon monoxide-free hydrogen production via low-temperature steam reforming of ethanol over iron-promoted Rh catalyst, *J. Catal.* 276 (2010) 197–200.
- [7] C.K.S. Choong, L. Chen, Y. Du, Z. Wang, L. Hong, A. Borgna, Rh-Fe/Ca-Al<sub>2</sub>O<sub>3</sub>: a unique catalyst for CO-free hydrogen production in low temperature ethanol steam reforming, *Top. Catal.* 57 (2014) 627–636.
- [8] C.K.S. Choong, L. Chen, Y. Du, M. Schreyer, S.W. Daniel Ong, C.K. Poh, L. Hong, A. Borgna, The role of metal-support interaction for CO-free hydrogen from low temperature ethanol steam reforming on Rh-Fe catalysts, *Phys. Chem. Chem. Phys.* 19 (2017) 4199–4207.
- [9] T. Fukushima, Y. Ishii, Y. Onda, M. Ichikawa, Promoting role of Fe in enhancing activity and selectivity of MeOH production from CO and H<sub>2</sub> catalysed by SiO<sub>2</sub>-supported Ir, *J. Chem. Soc. Chem. Comm.* (24) (1985) 1752–1754.
- [10] M.M. Bhasin, W.J. Bartley, P.C. Ellgen, T.P. Wilson, Synthesis gas conversion over supported rhodium and rhodium-iron catalysts, *J. Catal.* 54 (1978) 120–128.
- [11] R.L. Garten, J.H. Sinfelt, Structure of Pt-Ir catalysts: Mössbauer spectroscopy studies employing <sup>57</sup>Fe as a probe, *J. Catal.* 62 (1980) 127–139.
- [12] D.C. Koningsberger, C.P.J.H. Borgmans, A.M.J. van Elderen, B.J. Kip, J. W. Niemantsverdriet, Methanol from synthesis gas over iron-rich iron–iridium on silica catalysts, *J. Chem. Soc. Chem. Comm.* (12) (1987) 892–894.
- [13] A. Fukuoka, T. Kimura, N. Kosugi, H. Kuroda, Y. Mina, Y. Sakai, T. Tominaga, M. Ichikawa, Bimetallic promotion of alcohol production in CO hydrogenation and olefin hydroformylation on RhFe, PtFe, PdFe, and IrFe cluster-derived catalysts, *J. Catal.* 126 (1990) 434–450.
- [14] K. Liu, A. Wang, W. Zhang, J. Wang, Y. Huang, J. Shen, T. Zhang, Quasi in situ <sup>57</sup>Fe Mössbauer spectroscopic study: quantitative correlation between Fe<sup>2+</sup> and H<sub>2</sub> concentration for PROX over Ir–Fe/SiO<sub>2</sub> catalyst, *J. Phys. Chem. C* 114 (2010) 8533–8541.
- [15] L.J. Swartzendruber, The Fe-Ir (Iron-Iridium) system, *Bull. Alloy Ph. Diagr.* 5 (1984) 48–52.
- [16] L.M.P. van Gruijthuijsen, G.J. Howsmon, W.N. Delgass, D.C. Koningsberger, R. A. van Santen, J.W. Niemantsverdriet, Structure and reactivity of bimetallic Fe/Ir/SiO<sub>2</sub> catalysts after reduction and during high-pressure CO hydrogenation, *J. Catal.* 170 (1997) 331–345.
- [17] T. Lu, J. Lin, X. Liu, X. Wang, T. Zhang, Structure evolution and hydrogenation performance of IrFe bimetallic nanomaterials, *Langmuir* 32 (2016) 2771–2779.
- [18] E.L. Kunkes, D.A. Simonetti, J.A. Dumesci, W.D. Pyrz, L.E. Murillo, J.G. Chen, D. J. Buttrey, The role of rhenium in the conversion of glycerol to synthesis gas over carbon supported platinum–rhenium catalysts, *J. Catal.* 260 (2008) 164–177.
- [19] L. He, Y. Huang, X.Y. Liu, L. Li, A. Wang, X. Wang, C.-Y. Mou, T. Zhang, Structural and catalytic properties of supported Ni–Ir alloy catalysts for H<sub>2</sub> generation via hydrous hydrazine decomposition, *Appl. Catal. B: Environ.* 147 (2014) 779–788.
- [20] N. Pino, S. Sithisa, Q. Tan, T. Souza, D. López, D.E. Resasco, Structure, activity, and selectivity of bimetallic Pd-Fe/SiO<sub>2</sub> and Pd-Fe/γ-Al<sub>2</sub>O<sub>3</sub> catalysts for the conversion of furfural, *J. Catal.* 350 (2017) 30–40.
- [21] P. Carrillo, R. Shi, K. Teeluck, S.D. Senanayake, M.G. White, In situ formation of FeRh nanoalloys for oxygenate synthesis, *ACS Catal.* 8 (2018) 7279–7286.
- [22] J. Kim, W.H. Park, W.H. Doh, S.W. Lee, M.C. Noh, J.-J. Gallet, F. Bournel, H. Kondoh, K. Mase, Y. Jung, B.S. Mun, J.Y. Park, Adsorbate-driven reactive interfacial Pt-Ni<sub>1-x</sub> nanostructure formation on the Pt<sub>3</sub>Ni(111) alloy surface, *Sci. Adv.* 4 (2018) 1–7.
- [23] A. Haryanto, S. Fernando, N. Murali, S. Adhikari, Current status of hydrogen production techniques by steam reforming of ethanol: a review, *Energy Fuels* 19 (2005) 2098–2106.
- [24] J. Lin, L. Chen, C.K.S. Choong, Z. Zhong, L. Huang, Molecular catalysis for the steam reforming of ethanol, *Sci. China Chem.* 58 (2015) 60–78.
- [25] J. Llorca, P.R. Piscina, J. Dalmon, J. Sales, N. Homs, CO-free hydrogen from steam-reforming of bioethanol over ZnO-supported cobalt catalysts effect of the metallic precursor, *Appl. Catal. B: Environ.* 43 (2003) 355–369.
- [26] J. Llorca, N. Homs, J. Sales, J.G. Fierro, P.R. Piscina, Effect of sodium addition on the performance of Co-ZnO-based catalysts for hydrogen production from bioethanol, *J. Catal.* 222 (2004) 470–480.
- [27] V.A. O’Shea, R. Nafría, P.R. Piscina, N. Homs, Development of robust Co-based catalysts for the selective H<sub>2</sub>-production by ethanol steam-reforming. The Fe-promoter effect, *Int. J. Hydrol. Energy* 33 (2008) 3601–3606.
- [28] Y. Chen, Z. Shao, N. Xu, Ethanol steam reforming over Pt catalysts supported on Ce<sub>x</sub>Zr<sub>1-x</sub>O<sub>2</sub> prepared via a glycine nitrate process, *Energy Fuels* 22 (2008) 1873–1879.
- [29] H. Roh, Y. Wang, D.L. King, A. Platon, Y. Chin, Low temperature and H<sub>2</sub> selective catalysts for ethanol steam reforming, *Catal. Lett.* 108 (2006) 15–19.
- [30] N.J. Divins, I. Angurell, C. Escudero, V. Pérez-Dieste, J. Llorca, Influence of the support on surface rearrangements of bimetallic nanoparticles in real catalysts, *Science* 346 (2014) 620.
- [31] K.J. Andersson, F. Calle-Vallejo, J. Rossmeisl, I. Chorkendorff, Adsorption-driven surface segregation of the less reactive alloy component, *J. Am. Chem. Soc.* 131 (2009) 2404–2407.
- [32] Y. Du, Y. Zhu, S. Xi, P. Yang, H.O. Moser, M.B.H. Breese, A. Borgna, XAFCA: a new XAFS beamline for catalysis research, *J. Syn. Radiat.* 22 (2015) 839–843.
- [33] J. Sun, A.M. Karim, D. Mei, M. Engelhard, X. Bao, Y. Wang, New insights into reaction mechanisms of ethanol steam reforming on Co-ZrO<sub>2</sub>, *Appl. Catal. B: Environ.* 162 (2015) 141–148.
- [34] W. Zhang, A. Wang, L. Li, X. Wang, T. Zhang, Design of a novel bifunctional catalyst IrFe/Al<sub>2</sub>O<sub>3</sub> for preferential CO oxidation, *Catal. Today* 131 (2008) 457–463.
- [35] G.K. Wertheim, H.J. Guggenheim, Conduction-electron screening in metallic oxides: IrO<sub>2</sub>, *Phys. Rev. B* 22 (1980) 4680–4683.
- [36] R. Ferrando, J. Jellinek, R.L. Johnston, Nanoalloys: from theory to applications of alloy clusters and nanoparticles, *Chem. Rev.* 108 (2008) 845–910.
- [37] R.W. Joyner, R.A. van Santen, Elementary Reaction Steps in Heterogeneous Catalysis. In *Elementary Reaction Steps in Heterogeneous Catalysis*, Eds. Springer Netherlands: Dordrecht, 1993; pp 1–2.
- [38] H.F.J. Van't Blik, J.B.A.D. Van Zon, T. Huizinga, J.C. Vis, D.C. Koningsberger, R. Prins, An extended x-ray absorption fine structure spectroscopy study of a highly dispersed rhodium/aluminum oxide catalyst: the influence of carbon monoxide chemisorption on the topology of rhodium, *J. Phys. Chem.* 87 (1983) 2264–2267.
- [39] F. Solymosi, E. Novak, A. Molnar, Infrared spectroscopic study on carbon monoxide-induced structural changes of iridium on an alumina support, *J. Phys. Chem.* 94 (1990) 7250–7255.
- [40] F. Solymosi, M. Pasztor, An infrared study of the influence of carbon monoxide chemisorption on the topology of supported rhodium, *J. Phys. Chem.* 89 (1985) 4789–4793.
- [41] N. Kruse, A. Gaussmann, CO-induced morphological changes of Rh crystallites: mechanisms, kinetics, and real-space imaging on the atomic scale, *J. Catal.* 144 (1993) 525–543.
- [42] K. Balasubramanian, Electronic states of Pt<sub>2</sub>, *J. Chem. Phys.* 87 (1987) 6573–6578.
- [43] H.Y. Sang, A.D. David, B.A. James, O. Pablo, G. Keith, Density functional studies of small platinum clusters, *J. Phys.: Condens. Matter* 9 (1997) L39.
- [44] L. Xiao, L. Wang, Structures of platinum clusters: Planar or Spherical? *J. Phys. Chem. A* 108 (2004) 8605–8614.
- [45] B. Qiao, A. Wang, X. Yang, L.F. Allard, Z. Jiang, Y. Cui, J. Liu, J. Li, T. Zhang, Single-atom catalysis of CO oxidation using Pt<sub>1</sub>/FeO<sub>x</sub>, *Nat. Chem.* 3 (2011) 634.